Check for updates

Advanced Materials

ADVANCED MATERIALS
www.advmat.de

RESEARCH ARTICLE

Separation of Hydrogen and Graphite from Natural Gas Through Nickel Atomic Lattice

Mengze Zhao[1] | Zhibin Zhang[1] | Cong Wang[1] | Peng Feng[2] | Kuan Yang[2] | Mingchao Ding[3] | Yuheng Jiang[4] | Quanlin Guo[1] | Meng Wang[5] | Muhong Wu[6,7] | Guangyu Zhang[3] | Xin-Zheng Li[1,6] | Zhiyong Tang[4] | Ding Ma[5] | Zhipeng Li[2] | Enge Wang[8] | Kaihui Liu[1,7,8]

[1]State Key Laboratory for Mesoscopic Physics, Frontiers Science Center For Nano-optoelectronics, School of Physics, Peking University, Beijing, China | [2]Frontiers Science Center for Flexible Electronics, Northwestern Polytechnical University, Xi'an, China | [3]Institute of Physics, Chinese Academy of Sciences, Beijing, China | [4]Center for Excellence in Nanoscience, National Center for Nanoscience and Technology, Beijing, China | [5]College of Chemistry and Molecular Engineering, Peking University, Beijing, China | [6]Interdisciplinary Institute of Light-Element Quantum Materials and Research Center For Light-Element Advanced Materials, Peking University, Beijing, China | [7]Songshan Lake Materials Laboratory, Dongguan, China | [8]International Center For Quantum Materials, Collaborative Innovation Centre of Quantum Matter, Peking University, Beijing, China

Correspondence: Ding Ma (dma@pku.edu.cn) | Zhipeng Li (iamzpli@nwpu.edu.cn) | Enge Wang (egwang@pku.edu.cn) | Kaihui Liu (khliu@pku.edu.cn)

Received: 19 September 2025 | **Revised:** 21 January 2026 | **Accepted:** 3 February 2026

Keywords: graphite | hydrogen generation | natural gas utilization

ABSTRACT

The sustainable use of fossil fuels requires simultaneous efficient utilization of both energy and matter. Traditional fossil fuel processes primarily harvest energy through combustion, leaving much of the matter—especially carbon—unexploited and released in the form of greenhouse gas (carbon dioxide). Here, we develop an atomic lattice separation method using a nickel foam-nickel foil structure to simultaneously extract both energy and matter from natural gas with high efficiency. In this design, hydrogen in natural gas is catalytically converted to hydrogen gas on nickel foam, while carbon is transformed into crystalline graphite via transport through the atomic lattice of nickel foil. This approach achieved efficient (> 99% conversion), stable (≥ 300 h stability), and reusable (≥ 5 cycles) hydrogen gas generation, coupled with the production of high-value graphite with an ultrahigh crystal quality and superior thermal and electrical properties. Further integration with a solid oxide fuel cell system demonstrated an electricity generation efficiency of ~57%. This strategy establishes a sustainable pathway for separating energy (hydrogen) and matter (graphite) from hydrocarbons, thus providing new opportunities for high-efficiency and zero-emission natural gas utilization.

1 | Introduction

The year 2024 was the hottest year on record since 1850 and has breached the Paris Agreement 1.5°C threshold for the first time [1, 2], primarily driven by the rising greenhouse gas (mainly carbon dioxide, CO_2) emissions [3–5]. More than 90% of these emissions are attributed to fossil fuel consumption [6], highlighting the urgent need to transition toward a sustainable energy system. The separation of carbon from fossil fuels, particularly natural gas, which accounts for 30% of fossil energy consumption, has attracted significant attention because it enables low-cost and zero-emission production of hydrogen gas (H_2) [7–12]. By separating carbon from natural gas and fixing it in a solid form through pyrolysis rather than combusting it into CO_2, up to 7.5 billion tons

Mengze Zhao, Zhibin Zhang, Cong Wang, and Peng Feng contributed equally to this work.

© 2026 Wiley-VCH GmbH

of CO_2 emissions could potentially be eliminated annually [13]. If the separated carbon products also have substantial commercial value, this CO_2-free strategy would become an economically compelling cornerstone, stimulating the widespread adoption of low-carbon energy practices and significantly contributing to the goal of sustainable development [14–16].

In recent years, extensive efforts have been devoted to carbon separation and utilization processes [17–19], including catalyst development [20], reactor engineering [21], system integration [22], and environmental assessment [23]. Despite these advances, achieving controllable hydrogen–carbon separation from natural gas faces significant challenges that hinder its industrial application: (i) Achieving a high efficiency requires catalysts with large specific surface areas, which are typically in the form of powder or porous materials [24]. As a result, the carbon products formed on these catalysts are predominantly amorphous or microcrystalline, significantly limiting the value of the obtained carbon materials [25, 26]. (ii) H_2 generation and carbon production typically both occur on the catalyst surface, leading to the accumulation of solid amorphous carbon (coke). The formed coke tends to block catalytic sites, and more importantly, it is difficult to separate from the catalysts [27–29]. Consequently, catalyst deactivation limits the duration of steady-state operation of such processes to generally within 20 h [30–32]. Recently, molten alloy and molten salt catalysts have been developed to enhance the stability through the removal of carbon products that float on top of molten catalysts, but balancing the quality of the carbon products in a dynamically flowing environment remains challenging [9, 10, 19, 33]. To realize the ultimate goal of hydrogen–carbon separation from natural gas, it is crucial to design better pathways capable of simultaneously offering valuable carbon products, a high H_2 generation efficiency, and enhanced reaction stability.

Here, we developed an atomic lattice separation method using a tubular nickel (Ni) foam-Ni foil structure to separate the energy (hydrogen) and matter (carbon) conversion pathways in natural gas (Figure 1a,b; Figure S1). In this method, the Ni foam with a large specific surface area acts as the catalyst for natural gas pyrolysis, ensuring high efficiency in H_2 production and the formation of active carbon species. The crystalline Ni lattice functions as an atomic-scale separation and transport medium: carbon atoms generated during CH_4 decomposition dissolve into the Ni lattice, diffuse through it, and subsequently precipitate as crystalline graphite on the opposite surface (Figure 1c and Figure S2). This spatial separation of hydrogen and graphite formation decouples the energy conversion (H_2 production) from matter fixation (solid carbon formation). For H_2 production, sustained precipitation of graphite effectively consumes the amorphous carbon accumulated on the Ni foam surface and thereby maintains the catalytic activity. For solid carbon formation, the Ni lattice effectively blocks impurity elements and enables the epitaxial growth of high-quality crystalline graphite [34], whose value is substantially higher than that of conventional amorphous carbon byproducts. As a result, this method enables both stable pyrolysis of natural gas into H_2 and continuous production of crystalline graphite, significantly improving the energy conversion efficiency and the economic value of the products.

2 | Results and Discussion

2.1 | Design for Atomic Lattice Separation of Hydrogen Gas and Graphite

In our experiment, the Ni foam-Ni foil structure was first fabricated and loaded into the pyrolysis system to create separate inner and outer environments (Figure 1a and Figure S1). Here, the separation of the inner and outer tubes was achieved by the airtightness between the Ni tube and the inner tube (see Methods for more details). Natural gas (93.5% CH_4, 4.6% other hydrocarbons, 1.2% N_2, and 0.7% CO_2) was fed into the inner tube, which served as the raw material for the production of H_2 and graphite, whereas protective N_2 was fed into the outer tube to prevent the oxidation of the Ni foil (Figure 1b,c).

With the independent inner and outer tube design, high-quality graphite grew on the outer Ni foil surface via the transport of carbon atoms through the Ni atomic lattice [34]. In our experiment, the crystalline graphite reached an area of 12 cm × 8 cm (Figure 1d). Moreover, H_2 was generated by the catalytic pyrolysis of natural gas on the Ni foam within the inner tube. The transformation from natural gas to H_2 was clearly visualized by plasma glow tests, with most of the input natural gas (shown as a pink plasma glow) being converted into H_2 (shown as a purple plasma glow) (Figure 1e).

2.2 | Continuous Production of High-Quality Graphite

Currently, most carbon products derived from natural gas pyrolysis are low-quality amorphous carbon, limiting the overall economic efficiency of the process. In this work, we utilized the inner side of the Ni foil to absorb active carbon species catalyzed by Ni foam and grow high-quality graphite on the outer side of the Ni foil in a crystalline form (Figure 2a). The highly active carbon species formed from gaseous carbon sources enable continuous epitaxial growth of large-scale high-quality graphite at a temperature significantly lower than previous works (~1100°C vs. 1300°C– 3000°C) [34–36]. The cross-sectional scanning electron microscopy (SEM) image and energy dispersive spectroscopy (EDS) maps of the Ni foil-graphite structure after reaction clearly demonstrate the epitaxial growth of high-quality graphite (Figure 2b).

The atomic lattice separation system enables the continuous growth of graphite over extended durations. Graphite thicknesses obtained at different reaction times show a well-defined growth behavior, with an average growth rate of ~0.3 μm·h^{-1} (~1000 layers·h^{-1}, Figure S3). The interfacial growth through the Ni lattice also ensured that each graphene layer nucleated epitaxially on the Ni surface, thereby maintaining the crystallinity. In addition, the growth side was exposed to N_2, which provided a chemically inert and stable environment that further supported uniform crystal formation. Both Raman spectroscopy and X-ray diffraction (XRD) 2θ-scan confirmed its excellent crystal quality, with no defect-induced Raman D peak or surface orientations other than (0002) (Figure 2c,d). Electron backscatter diffraction (EBSD) characterization demonstrated its single crystallinity,

15214095, 0, Downloaded from https://advanced.onlinelibrary.wiley.com/doi/10.1002/adma.202518450 by Peking University Health, Wiley Online Library on [12/02/2026]. See the Terms and Conditions (https://onlinelibrary.wiley.com/terms-and-conditions) on Wiley Online Library for rules of use; OA articles are governed by the applicable Creative Commons License

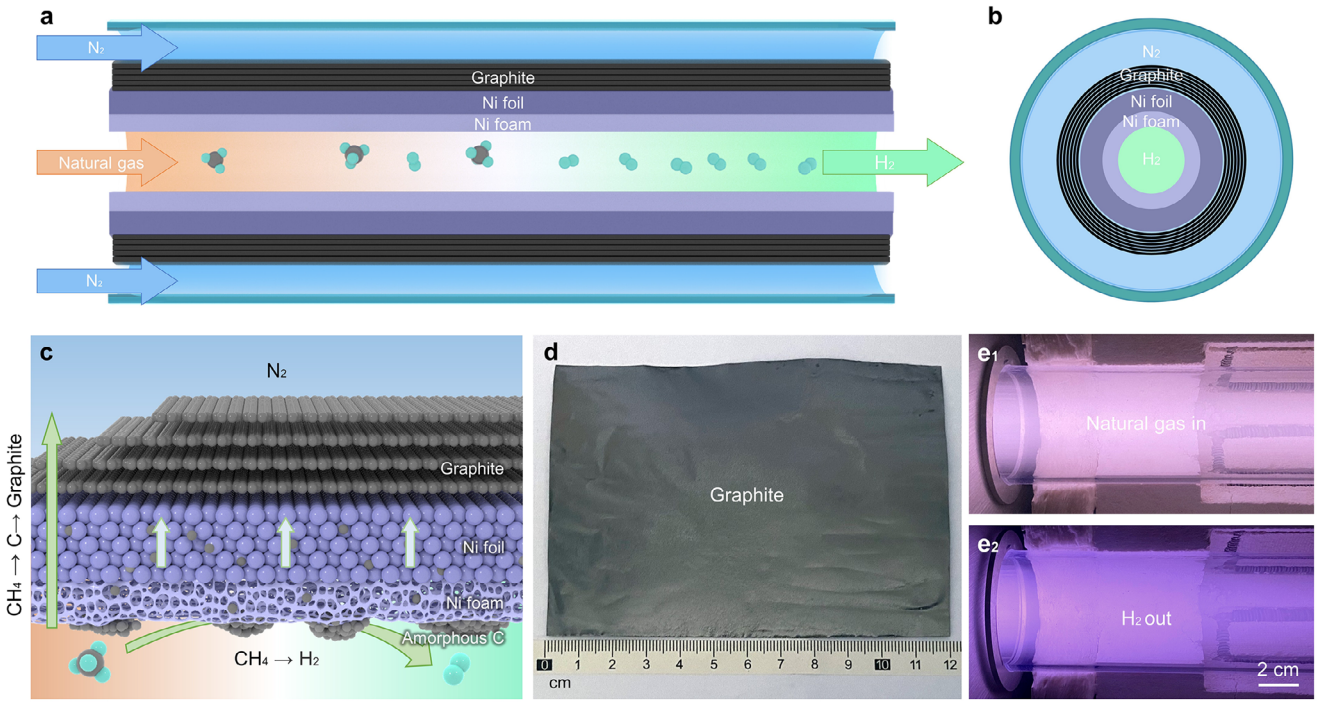

FIGURE 1 | Design of atomic lattice separation of H_2 and graphite from natural gas. a,b) Schematic of the atomic lattice separation method with separate inner and outer tubes (cross-sectional front view (a) and side view (b)). The inner and outer tubes are divided by the Ni foam-Ni foil structure, and natural gas passes through the inner tube while N_2 passes through the outer tube, with H_2 and graphite obtained as products. c) Schematic of the mechanism of the energy and matter transformation processes: (i) hydrogen atoms in natural gas transform into H_2 catalyzed by Ni foam; (ii) carbon atoms in natural gas transform into active amorphous carbon on Ni foam and finally form crystalline graphite on the outer side of the Ni foil via lattice transport. Here, only CH_4 from natural gas is depicted for clarity. d) Photograph of the large-scale high-quality crystalline graphite, with an area of up to 12 cm × 8 cm. e) Photograph of the characteristic plasma glow of the input natural gas (e_1) and output H_2 (e_2).

with an in-plane domain size exceeding 0.3 mm (Figure S4a,b) and an out-of-plane orientation across the entire thickness of the graphite layer (Figure S4c,d). The in-plane lattice structure was also confirmed by high-resolution atomic force microscopy (AFM, Figure S4e). Cross-sectional scanning transmission electron microscopy (STEM) further revealed its perfect Bernal (AB) stacking with an interplanar distance of 0.335 nm (Figure 2e), which precisely aligned with the theoretical value [37] and was also confirmed by the high-resolution XRD (Figure S4f).

The as-grown graphite also had a high purity. The atomic lattice separation method facilitated the transport of carbon atoms, while other impurity elements were effectively blocked because of their high absorption, diffusion, or precipitation barriers in Ni. As a result, the obtained crystalline graphite demonstrated ultrahigh purity, as indicated by inductively coupled plasma–mass spectrometry (ICP–MS) analysis with an impurity density of ~10 ppm. This purity is superior to that of commercially available high-quality highly oriented pyrolytic graphite (HOPG, with a purity of ~100 ppm) (Figure 2f). It should further be noted that this impurity-filtering effect would also lead to gradual impurity accumulation within the Ni lattice, which can slightly reduce the graphite growth rate at extended time-scale (Figure S3). Therefore, further improvement in impurity control would be beneficial for sustaining long-term growth.

The excellent crystallinity and ultrahigh purity of the obtained graphite endow it with superior physical properties. Thermal measurements revealed that our graphite film exhibited a thermal conductivity of ~1750 $W \cdot m^{-1} \cdot K^{-1}$, surpassing that of other commercial graphite film products tested under the same conditions (Figure 2g). Moreover, the as-grown graphite could also be used for the exfoliation of monolayer graphene and, therefore, exploration of intrinsic quantum properties. Here, we fabricated a quantum Hall device using exfoliated monolayer graphene from crystalline graphite, and quantum transport measurements revealed a high-resolution quantum Landau fan diagram with integer filling states of $\nu = \pm 2, \pm 6, \pm 10, \ldots$, and a carrier mobility of ~200 000 $cm^2 \cdot V^{-1} \cdot s^{-1}$ (Figure 2h and Figure S5), demonstrating its exceptional electrical quality.

2.3 | Effective Production of Hydrogen Gas with High Stability

As carbon is separated from natural gas, the residual hydrogen atoms are then converted into H_2 within the inner tube. With our Ni foam-Ni foil design, both a high conversion efficiency and excellent stability were achieved. The high conversion efficiency (~80% for CH_4 and >90% for C_2H_6 and C_3H_8, Figure 3a) results from the low reaction barrier (deduced from the Arrhenius fitting to be ~156 $kJ \cdot mol^{-1}$ for CH_4, Figure 3b and Figure S6a) and the large specific surface area provided by the Ni foam catalyst. Moreover, benefiting from the continuous diffusion of active carbon species through the Ni atomic lattice transport, excessive carbon accumulation on the catalytic Ni foam surface

15214095, 0, Downloaded from https://advanced.onlinelibrary.wiley.com/doi/10.1002/adma.202518450 by Peking University Health, Wiley Online Library on [12/02/2026]. See the Terms and Conditions (https://onlinelibrary.wiley.com/terms-and-conditions) on Wiley Online Library for rules of use; OA articles are governed by the applicable Creative Commons License

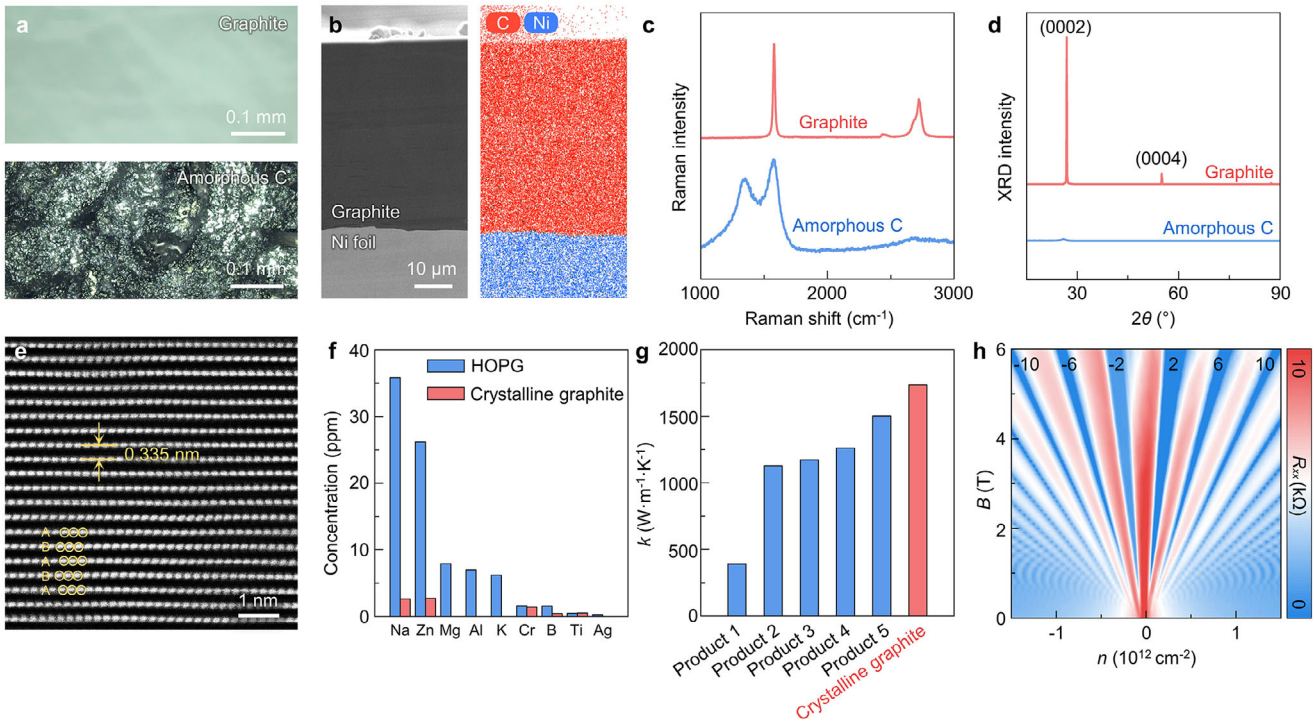

FIGURE 2 | Characterizations of high-quality crystalline graphite. a) Optical image of the crystalline graphite on the outer side of the Ni foil (top panel) and the amorphous carbon (amorphous C) on the inner side of the Ni foam (bottom panel). b) Cross-sectional SEM image (left panel) and EDS maps (right panel) of the crystalline graphite grown on the Ni foil, with a thickness of ~50 μm. c,d) Raman spectra (c) and XRD 2θ-scan (d) of the obtained crystalline graphite and amorphous carbon. e) Cross-sectional STEM image of the crystalline graphite, showing a perfect Bernal (AB) stacked structure with an interlayer distance of 0.335 nm. f) ICP–MS analysis of the crystalline graphite and HOPG. g) Thermal conductivities of the crystalline graphite and 5 kinds of commercial graphite film products. h) Quantum Landau fan diagram of an exfoliated monolayer graphene device, showing the longitudinal resistance (R_{xx}) as a function of the carrier density (n) and perpendicular magnetic field (B).

is effectively eliminated, resulting in exceptional operational stability exceeding 300 h (Figure 3c, top panel, and Figure S6b). This suppression of coke buildup also allows the Ni foam-Ni foil structure to be reused for more than 5 cycles, demonstrating the reusability and sustainability potential of our design (Figure 3c, bottom panel, and Figure S6c).

The conversion efficiency of natural gas could be further improved by employing a cascade system in which natural gas sequentially passes through two atomic lattice separation processes (with the output gases after the first and second stages denoted as Out-1 gas and Out-2 gas, respectively) (Figure 3d). A final CH_4 conversion exceeding 99% and H_2 production rate of ~3200 mL·h^{-1} was realized, with the CH_4 content decreasing from 93.5% in natural gas to 0.2% in Out-2 gas (Figure 3e and Table S1). In addition, the small amount of CO_2 in natural gas also decreased (from 0.7% in natural gas to < 0.01% in Out-2 gas), with a simultaneous increase in carbon monoxide (CO, from 0% in natural gas to 0.7% in Out-2 gas, Table S1). The changes in the gas composition in terms of CO_2 and CO indicate the occurrence of a dry reforming reaction (i.e., $CO_2 + CH_4 \rightarrow 2CO + 2H_2$) in our system, which is also beneficial for energy generation [38]. Besides, because the natural gas content is significantly reduced before entering the second stage, the second atomic lattice separation process is easier to maintain stability. The overall stability of the cascade system thus depends on the first atomic lattice separation process and could also reach ≥ 300 h. Overall, the high conversion efficiency and high stability of the reaction of natural gas into H_2, together with high-value carbon products (graphite), make the proposed method a potentially economical way to utilize the energy and matter of natural gas (Figure 3f) [7–12].

2.4 | Integrated Atomic Lattice Separation and Solid Oxide Fuel Cell System

Given the challenges in storing and transporting H_2, an optimal approach to use the generated H_2 is to directly convert it into electricity. This conversion can be achieved via (i) direct combustion or (ii) electrochemical reactions. The combustion efficiency is generally constrained by Carnot's theorem, whereas electrochemical reactions can circumvent this limitation [39]. Thus, electrochemical reactions realized through fuel cells are regarded as effective ways to utilize hydrogen energy. Here, to achieve direct electric power generation, we integrated our atomic lattice separation system with a custom-designed solid oxide fuel cell unit (SOFC, known for its high efficiency, low cost, and long lifespan) (Figure 4a,b; Figure S7).

When Out-2 gas was used as the fuel, electric power could be immediately generated through the SOFC, successfully charging a mobile phone (Figure 4c). Owing to the fast oxidation kinetics and high electrochemical activity of H_2 at the electrode [40, 41], Out-2 gas could provide a maximum power density of 1.0 W·cm^{-2} (Figure 4d and Figure S8a). What's more, the efficient

15214095, 0, Downloaded from https://advanced.onlinelibrary.wiley.com/doi/10.1002/adma.202518450 by Peking University Health, Wiley Online Library on [12/02/2026]. See the Terms and Conditions (https://onlinelibrary.wiley.com/terms-and-conditions) on Wiley Online Library for rules of use; OA articles are governed by the applicable Creative Commons License

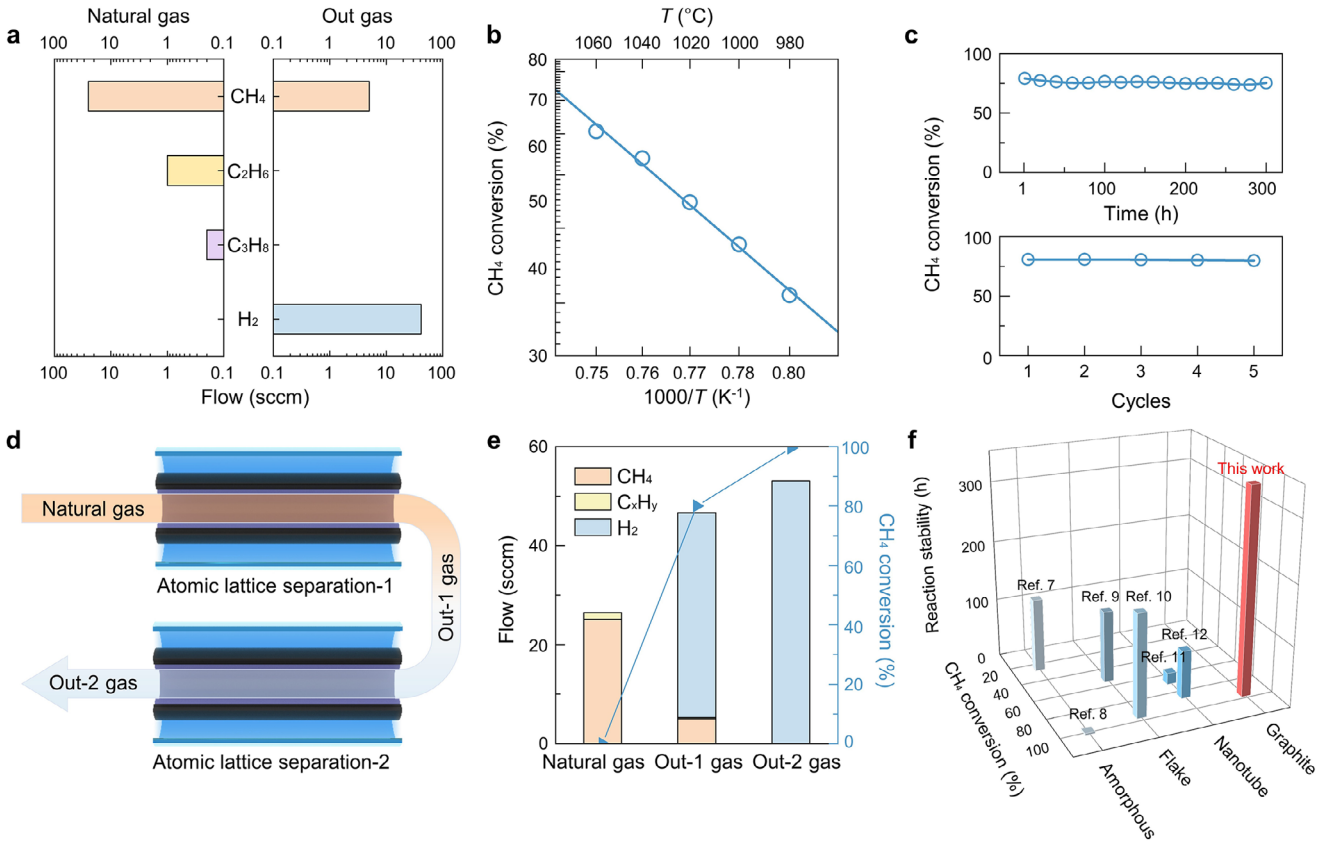

FIGURE 3 | The conversion and stability of H_2 generation. a) Typical gas composition before (natural gas) and after the lattice separation reaction at 1150°C. b) Relationship between CH_4 conversion and temperature (T), showing the effective activation energy (E_a = 156 kJ·mol^{-1}) of the atomic lattice separation process. c) Long-term stability (top panel) and cyclic stability (bottom panel) tests of the atomic lattice separation process at 1150°C. d) Schematic of the atomic lattice separation cascade system, the output gas of atomic lattice separation-1 (Out-1 gas) is used as the input gas of atomic lattice separation-2, with the final output denoted as Out-2 gas. e) The gas flow (columns) and CH_4 conversion (triangles) before and after each atomic lattice separation process. The unit of flow is standard cubic centimeters per minute (sccm). f) The comparison of different hydrogen–carbon separation designs, in terms of respective maxima for CH_4 conversion, carbon product types, and reaction stability.

anodic H_2 oxidation could also help to avoid local hot spots in the cell, and thus prevent thermal and mechanical stresses that may cause cell fracture (which is observed when fed with natural gas, Figure S9). Besides, the high H_2 purity in Out-2 gas could mitigate the heterogeneous reaction kinetics by avoiding carbon deposition and methane concentration variations [42–44], allowing the fuel cell using Out-2 gas to demonstrate a superior performance and stability for ≥ 300 h (Figure 4e). Furthermore, we measured the maximum effective gas flow of the cell (Figure S8b) and estimated an electricity generation efficiency of up to ~57%.

It is also worth noting that the electrochemical reaction in the SOFC is exothermic, thus typically producing heat when generating electricity. Since the natural gas pyrolysis process occurs at high temperatures and has a high energy demand, we propose that the heat from the SOFC could potentially be used to heat the natural gas before it enters the system and thus save energy in the pyrolysis reaction through a delicate heat-transfer system design [45, 46]. After refinement, this approach could in principle enable a net electricity output from natural gas, ideally producing ~3 kW·h of electricity and ~500 g of high-quality graphite and reducing CO_2 emission by ~2 kg for 1 m^3 of natural gas (Table S2).

3 | Conclusion

With the atomic lattice separation design, we simultaneously achieved continuous production of both green hydrogen and high-quality crystalline graphite, significantly improving the economic benefits (Table S3). Our system can also be directly integrated with fuel cells for high-efficiency electricity generation, providing an industrially feasible approach for sustainable power production from fossil fuels. In future developments, our design can be further advanced through purity control and upgraded reactor hardware specifically optimized for long-term high-temperature operation. In addition, other hydrocarbon sources (such as methane clathrate and associated petroleum gas) could potentially be incorporated into this approach to further enhance economic energy utilization.

4 | Experimental Section

4.1 | Continuous Production of H_2 and High-Quality Graphite

Ni foil (50 μm thick, 99.9% purity, Zhongke Crystal Materials Co. Ltd) and Ni foam (110 pores per inch, Zhongke Crystal

15214095, 0, Downloaded from https://advanced.onlinelibrary.wiley.com/doi/10.1002/adma.202518450 by Peking University Health, Wiley Online Library on [12/02/2026]. See the Terms and Conditions (https://onlinelibrary.wiley.com/terms-and-conditions) on Wiley Online Library for rules of use; OA articles are governed by the applicable Creative Commons License

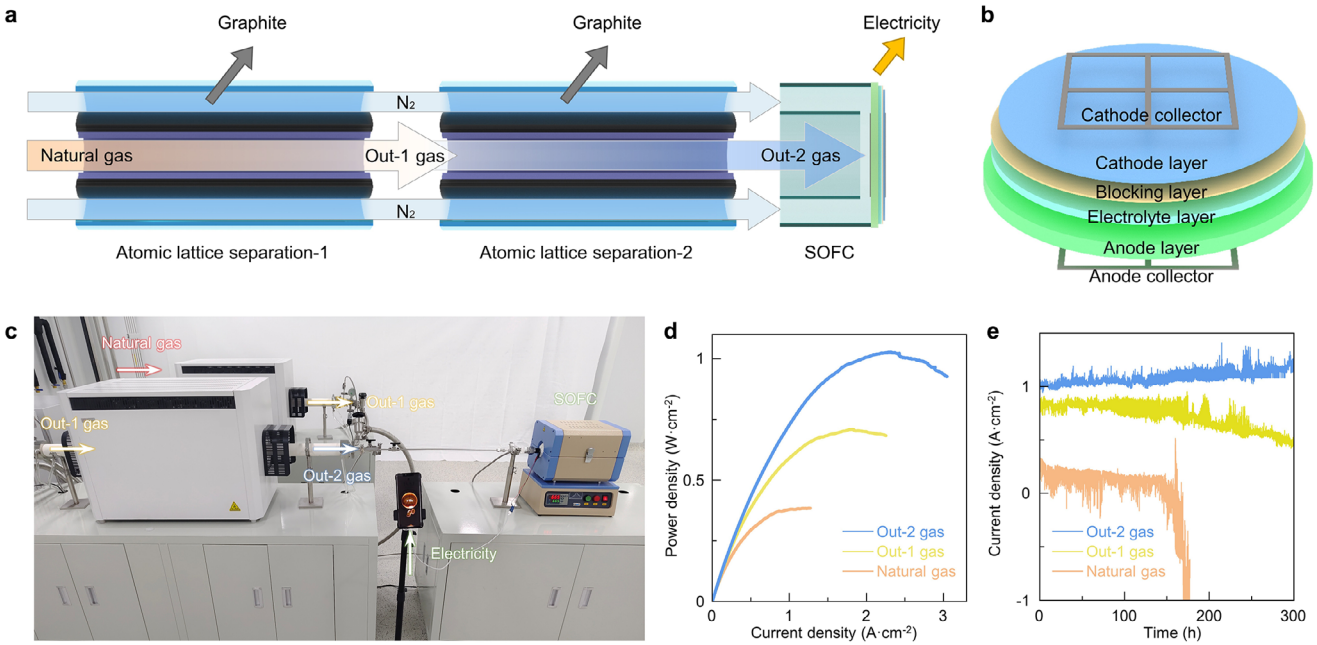

FIGURE 4 | Integrated atomic lattice separation and SOFC system. a–c) Schematic (a) and photograph (c) of the integrated two- stage atomic lattice separation processes and SOFC system, demonstrating a direct application of mobile phone charging. The structure of the SOFC is shown in (b). d,e) Power density (d) and stability (e) of the SOFC with natural gas, Out-1 gas, and Out-2 gas as inputs, demonstrating the highest power density of ~1 $W{\cdot}cm^{-2}$ and the highest stability of ≥ 300 h when using Out-2 gas. Here, the negative current signal under natural gas indicates the occurrence of cell failure.

Materials Co. Ltd) were first stacked and placed between two alumina plates, and then annealed at 1300°C for 5 h under a reducing atmosphere (800 sccm Ar, 100 sccm H_2) in a custom-designed chemical vapor deposition (CVD) furnace (Tianjin Kaiheng Co. Ltd). The area of the Ni foil was approximately 8 cm × 15 cm. Following this, the Ni foam-Ni foil structure was rolled and then annealed again at the same temperature and under identical atmospheric conditions. After this process, the commercial Ni foil was transformed into crystalline Ni foil with large domains. Both ends of the Ni roll were then bonded to the openings of the internal quartz or alumina tubes using a high-temperature adhesive (552 alumina adhesive, Ceramabond) to avoid gas permeation. The entire assembly was then loaded into the CVD furnace. After heating to 980°C–1150 °C, natural gas was introduced into the inner tube to facilitate the production of hydrogen and high-quality graphite. Finally, the system was allowed to cool naturally under the same protective atmosphere.

4.2 | Purity Measurements by ICP–MS

All sample preparation procedures were carried out in a clean laboratory environment to minimize contamination. Plastic tweezers, quartz digestion vessels, and plastic containers were pre-cleaned by soaking in 10% HNO_3 (North Weiye Measurement Group Co., Ltd.) for 12 h, followed by thorough rinsing with ultrapure water and air-drying. Graphite samples grown on Ni substrates were carefully peeled off using the acid-cleaned plastic tweezers. For comparison, the HOPG sample (SPI Supplies) was peeled off under the same conditions. The peeled graphite samples (~ 2–10 mg) were accurately weighed and transferred into microwave digestion vessels. Then, 0.75 mL of 14.4 $mol{\cdot}L^{-1}$ HNO_3 and 0.25 mL of 12 $mol{\cdot}L^{-1}$ HCl were added to the vessel, which was then placed in a micro-digester, and heated at 260°C for 1 h until the solution was transparent. After cooling, the obtained solution was diluted to the designed volume with deionized water. The impurity elements within the solution were then quantitatively analyzed by a PerkinElmer NexlON 350X ICP–MS.

4.3 | Thermal Conductivity Measurements by the Laser Flash Method

The in-plane thermal conductivity λ of graphite was determined by $\lambda = \alpha{\cdot}c_p{\cdot}\rho$, where the in-plane thermal diffusion coefficient α was quantified via laser flash method utilizing a Netzsch NETLFA 467 at a temperature of 25°C; the specific heat capacity c_p was measured employing a TA Instruments DSC 2500; the density ρ was adopted based on graphite's theoretical value of 2.25 $g{\cdot}cm^{-3}$.

4.4 | Fabrication of Quantum Hall Device and Transport Measurements

The device was fabricated with a modified dry transfer technique, where monolayer graphene was first exfoliated from our crystalline graphite onto a SiO_2/Si substrate, and then a polypropylene carbonate (PPC) film was employed to sequentially pick up an hBN flake (from bulk hBN crystals, Shanghai Onway Technology), the exfoliated monolayer graphene, and another hBN flake. This stack was then transferred onto a graphite flake positioned atop a SiO_2/Si substrate. After the assembly of the stack, a Hall

15214095, 0, Downloaded from https://advanced.onlinelibrary.wiley.com/doi/10.1002/adma.202518450 by Peking University Health, Wiley Online Library on [12/02/2026]. See the Terms and Conditions (https://onlinelibrary.wiley.com/terms-and-conditions) on Wiley Online Library for rules of use; OA articles are governed by the applicable Creative Commons License

bar pattern was defined on the top hBN layer utilizing electron-beam lithography with polymethyl methacrylate (PMMA) as the photoresist. Reactive ion etching (CHF_3:O_2 = 30:3) was then utilized to remove the top hBN layer outside the masked areas, thereby exposing the edges of the graphene layer beneath. Electrical contacts were established by deposition of 5 nm chromium and 80 nm gold via electron-beam evaporation. The electrical properties of the device were assessed through four-terminal transport measurements carried out at a temperature of 1.7 K within a 9 T superconducting magnet system.

4.5 | Measurement of Gas Composition and Stability Tests for Natural Gas Pyrolysis

Gas composition was quantified using an Agilent ADM flow meter to measure total gas flow and a Shimadzu GC-2014C gas chromatograph equipped with a flame ionization detector, thermal conductivity detector, and methanizer after Porapak-N and Molesieve-13X columns and rotary valves. The gases used for testing were collected after stabilizing for half an hour under steady conditions. During stability, cycling, and cascade testing, the temperature was maintained at 1150°C with a constant natural gas feed of 26.5 sccm. For the cycling tests, the natural gas supply was stopped after each cycle, and residual gas in the inner tube was cleaned using N_2. The system was then cooled to room temperature under a N_2 atmosphere, and the outside epitaxial graphite was exfoliated before the next cycle.

4.6 | Assembly of SOFC

All powders (NiO, 8% yttria-stabilized zirconia (YSZ), 20% gadolinium-doped ceria oxide (GDC), $La_{0.6}Sr_{0.4}Co_{0.2}Fe_{0.8}O_{3-\delta}$(LSCF)) were synthesized via a standardized Pechini sol-gel method [47–49]. All raw materials were sourced from Aladdin Chemical Reagent Company with 99.9% purity. Then the powders were used to fabricate the cell. First, Anode supports were fabricated by uniaxially pressing 0.4 g ball-milled NiO-YSZ-starch (mass ratio 6:4:2) powder into a green anode pellet with a diameter of 20 mm, followed by sintering at 1000°C for 5 h. Second, three layers of YSZ electrolyte and one layer of GDC barrier layer were screen-printed successively onto the anode and sintered at 1400°C for 5 h (electrolyte ~20 μm, barrier ~6 μm). The LSCF/GDC (7:3) cathode was then applied and sintered at 1000°C for 2 h (~50 μm). Third, conductive silver paste (DAD-87) current collectors were applied to the surface of the anode and cathode, ensuring swift current collection. Each coated layer was then subjected to a series of sintering and drying processes to enhance the mechanical robustness and electrical conductivity of the layers and to eliminate any residual moisture. Finally, the cell was integrated with the current collectors, forming a compact button-type single cell.

4.7 | Performance Tests of SOFC

During the tests of a single SOFC, the cell was encapsulated within a ceramic tube with a matching diameter to ensure an airtight environment. Two silver wires were led out from both sides of the SOFC single cell, then sealed at one end of the test reactor with Aremco 552 sealant, ensuring good airtightness and electrical contact. The fuel gas was introduced into the anode side of the SOFC, while the cathode side was exposed to the air. After stabilizing the system temperature at 700°C (monitored by three thermocouples at the center, edges, and between the surfaces of the single cell) and activated by feeding H_2. After activation, N_2 was fed for 30 min to completely replace H_2. Then, natural gas, Out-1, and Out-2 gases were introduced sequentially with the same cell to measure power density. Different cells were used in the stability test, but the alignment with the power test assured the consistency. Throughout these processes, real-time monitoring of output current and power was conducted to evaluate the cell's electrochemistry performance, and the voltage was controlled at 0.7 V. This voltage was subsequently elevated to around 5.0 V via a DC-DC boost converter for mobile phone charging applications. The generation efficiency can be calculated using the following equation:

$$\eta = \frac{E_{electricity}}{E_{effective}} = \frac{IV}{LHV \cdot F}$$

where η represents the power generation efficiency, I was the output current, V was the output voltage, LHV denotes the low calorific value of H_2, and F signifies the maximum effective gas flow rate. Five individual cells were connected in series to accurately determine the electrical conversion efficiency of the cell, and the effective H_2 flow rate for a single cell was derived from the total flow of the five connected cells.

4.8 | Characterizations

Optical images were obtained using an Olympus BX51 microscope. Raman spectra were obtained with a Witec alpha300 R system with a laser excitation wavelength of 514 nm and a power of 10 mW. The XRD 2θ-scan measurements were performed on a Bruker D8 Advance system. EBSD characterizations were performed using a PHI 710 Scanning Auger Nanoprobe. AFM images were acquired using Asylum Research Cypher S under ambient conditions. The cross-sectional graphite samples were prepared using a cross-section polisher (JEOL IB-19530). SEM images were obtained using an FEI Nova NanoSEM 430 scanning electron microscope. STEM experiments were performed in an FEI Titan Themis G2 300 operated at 300 kV.

Acknowledgements

This work was supported by the National Natural Science Foundation of China (Nos. 92577201, 52402043, 12427806, U24A20285, 11888101 and T2188101), Guangdong Major Project of Basic and Applied Basic Research (No. 2021B0301030002), and the New Cornerstone Science Foundation through the XPLORER PRIZE to K.L.

Conflicts of Interest

The authors declare no conflicts of interest.

Data Availability Statement

The data that support the findings of this study are available in the supplementary material of this article.

15214095, 0, Downloaded from https://advanced.onlinelibrary.wiley.com/doi/10.1002/adma.202518450 by Peking University Health, Wiley Online Library on [12/02/2026]. See the Terms and Conditions (https://onlinelibrary.wiley.com/terms-and-conditions) on Wiley Online Library for rules of use; OA articles are governed by the applicable Creative Commons License

References

1. World Meteorological Organization, *State of the Global Climate 2024*, Geneva, 2025, https://library.wmo.int/records/item/69075-state-of-the-climate-2024.

2. J. Tollefson, "Earth Breaches 1.5°C Climate Limit for the First Time: What Does it Mean?," *Nature* 637 (2025): 769–770, https://doi.org/10.1038/d41586-025-00010-9.

3. H. D. Matthews and S. Wynes, "Current Global Efforts are Insufficient to Limit Warming to 1.5°C," *Science* 376 (2022): 1404–1409, https://doi.org/10.1126/science.abo3378.

4. J. Rogelj, O. Geden, A. Cowie, and A. Reisinger, "Net-Zero Emissions Targets are vague: Three Ways to Fix," *Nature* 591 (2021): 365–368, https://doi.org/10.1038/d41586-021-00662-3.

5. Y. Cai, T. M. Lenton, and T. S. Lontzek, "Risk of Multiple Interacting Tipping Points Should Encourage Rapid CO_2 Emission Reduction," *Nature Climatic Change* 6 (2016): 520–525.

6. P. Erickson, M. Lazarus, and G. Piggot, "Limiting Fossil Fuel Production as the Next Big Step in Climate Policy," *Nature Climate Change* 8 (2018): 1037–1043, https://doi.org/10.1038/s41558-018-0337-0.

7. K. Wang, W. S. Li, and X. P. Zhou, "Hydrogen Generation by Direct Decomposition of Hydrocarbons Over Molten Magnesium," *Journal of Molecular Catalysis A: Chemical* 283 (2008): 153–157, https://doi.org/10.1016/j.molcata.2007.12.018.

8. L. Fulcheri, V. J. Rohani, E. Wyse, N. Hardman, and E. Dames, "An Energy-Efficient Plasma Methane Pyrolysis Process for High Yields of Carbon Black and Hydrogen," *International Journal of Hydrogen Energy* 48 (2023): 2920–2928, https://doi.org/10.1016/j.ijhydene.2022.10.144.

9. L. Chen, Z. Song, S. Zhang, et al., "Ternary NiMo-Bi Liquid Alloy Catalyst for Efficient Hydrogen Production From Methane Pyrolysis," *Science* 381 (2023): 857–861, https://doi.org/10.1126/science.adh8872.

10. D. C. Upham, V. Agarwal, A. Khechfe, et al., "Catalytic Molten Metals for the Direct Conversion of Methane to Hydrogen and Separable Carbon," *Science* 358 (2017): 917–921, https://doi.org/10.1126/science.aao5023.

11. X. Y. Lin, H. Zhu, M. Huang, C. S. Wan, D. L. Li, and L. L. Jiang, "Controlled Preparation of Ni–Cu Alloy Catalyst via Hydrotalcite-Like Precursor and its Enhanced Catalytic Performance for Methane Decomposition," *Fuel Processing Technology* 233 (2022): 107271, https://doi.org/10.1016/j.fuproc.2022.107271.

12. B. A. Al Alwan, M. Shah, M. Danish, M. K. Al Mesfer, M. I. Khan, and V. Natarajan, "Enhanced Methane Decomposition Over Transition Metal-Based Tri-Metallic Catalysts for the Production of CO_x Free Hydrogen," *Journal of the Indian Chemical Society* 99 (2022): 100393, https://doi.org/10.1016/j.jics.2022.100393.

13. *International Energy Agency*, *CO_2 Emissions in 2023*, Paris, 2024, https://www.iea.org/reports/co2-emissions-in-2023.

14. G. Chen, X. Tu, G. Homm, and A. Weidenkaff, "Plasma Pyrolysis for a Sustainable Hydrogen Economy," *Nature Reviews Materials* 7 (2022): 333–334, https://doi.org/10.1038/s41578-022-00439-8.

15. Y. F. Zhao, Z. Y. Shi, Y. L. Zhu, et al., "Mechanism for One-Pot Synthesis of 0D-2D Carbon Materials in the Bubbles Inside Molten Salts," *Advanced Functional Materials* 32 (2022): 2022381, https://doi.org/10.1002/adfm.202202381.

16. M. Abuseada and T. S. Fisher, "Continuous Solar-Thermal Methane Pyrolysis for Hydrogen and Graphite Production by Roll-to-Roll Processing," *Applied Energy* 352 (2023): 121872, https://doi.org/10.1016/j.apenergy.2023.121872.

17. C. Liang, Y. Chen, M. Wu, et al., "Green Synthesis of Graphite From CO Without Graphitization Process of Amorphous Carbon," *Nature Communication* 12 (2021): 119.

18. B. R. Luo, H. T. Liu, L. L. Jiang, et al., "Synthesis and Morphology Transformation of Single-Crystal Graphene Domains based on Activated Carbon Dioxide by Chemical Vapor Deposition," *Journal of Materials Chemistry C* 1 (2013): 2990–2995, https://doi.org/10.1039/c3tc30124a.

19. Y. Ji, C. Palmer, E. E. Foley, et al., "Valorizing the Carbon Byproduct of Methane Pyrolysis in Batteries," *Carbon* 204 (2023): 26–35.

20. S. Schneider, S. Bajohr, F. Graf, and T. Kolb, "State of the Art of Hydrogen Production via Pyrolysis of Natural Gas," *ChemBioEng Reviews* 7 (2020): 150–158, https://doi.org/10.1002/cben.202000014.

21. X. Zhang, J. Liu, W. D. Li, et al., "Methane Decomposition Enabled by Molten Alkali Chloride Electrolysis," *ACS Catalysis* 15 (2025): 3203–3214, https://doi.org/10.1021/acscatal.4c06377.

22. J. Peden, J. Ryley, J. Terrones, et al., "Production of Hydrogen and Carbon Nanotubes from Methane using a Multi-Pass Floating Catalyst Chemical Vapour Deposition Reactor With Process Gas Recycling," *Natural Energy* (2025): 1–14.

23. M. Keller, "Is Hydrogen Production Through Natural Gas Pyrolysis Compatible With Ambitious Climate Targets in the United States? A Location-Specific, Time-Resolved Analysis," *Environmental Research Letters* 17 (2022): 124017, https://doi.org/10.1088/1748-9326/aca553.

24. W. Xi, K. Wang, Y. Shen, et al., "Dynamic Co-Catalysis of Au Single Atoms and Nanoporous Au for Methane Pyrolysis," *Nature Communications* 11 (2020): 1919, https://doi.org/10.1038/s41467-020-15806-8.

25. P. Tang, Q. J. Zhu, Z. X. Wu, and D. Ma, "Methane Activation: The Past and Future," *Energy & Environmental Science* 7 (2014): 2580–2591, https://doi.org/10.1039/C4EE00604F.

26. J. Prabowo, L. Lai, B. Chivers, et al., "Solid Carbon co-Products From Hydrogen Production by Methane Pyrolysis: Current Understandings and Recent Progress," *Carbon* 216 (2024): 118507.

27. U. P. M. Ashik, W. M. A. W. Daud, and H. F. Abbas, "Production of Greenhouse Gas Free Hydrogen by Thermocatalytic Decomposition of Methane—A Review," *Renewable and Sustainable Energy Reviews* 44 (2015): 221–256, https://doi.org/10.1016/j.rser.2014.12.025.

28. T. V. Choudhary, E. Aksoylu, and D. W. Goodman, "Nonoxidative Activation of Methane," *Catalysis Reviews* 45 (2003): 151–203, https://doi.org/10.1081/CR-120017010.

29. T. Becker, M. Richter, and D. W. Agar, "Methane Pyrolysis: Kinetic Studies and Mechanical Removal of Carbon Deposits in Reactors of Different Materials," *International Journal of Hydrogen Energy* 48 (2023): 2112–2129, https://doi.org/10.1016/j.ijhydene.2022.10.069.

30. A. M. Amin, E. Croiset, C. Constantinou, and W. Epling, "Methane Cracking Using Ni Supported on Porous and Non-Porous Alumina Catalysts," *International Journal of Hydrogen Energy* 37 (2012): 9038–9048, https://doi.org/10.1016/j.ijhydene.2012.02.001.

31. A. Venugopal, S. N. Kumar, J. Ashok, et al., "Hydrogen Production by Catalytic Decomposition of Methane Over Ni/SiO_2Ni/SiO_2☆," *International Journal of Hydrogen Energy* 32 (2007): 1782–1788, https://doi.org/10.1016/j.ijhydene.2007.01.007.

32. M. A. Ermakova, D. Y. Ermakov, and G. G. Kuvshinov, "Effective Catalysts for Direct Cracking of Methane to Produce Hydrogen and Filamentous Carbon," *Applied Catalysis A: General* 201 (2000): 61–70, https://doi.org/10.1016/S0926-860X(00)00433-6.

33. B. Parkinson, C. F. Patzschke, D. Nikolis, S. Raman, D. C. Dankworth, and K. Hellgardt, "Methane Pyrolysis in Monovalent Alkali Halide Salts: Kinetics and Pyrolytic Carbon Properties," *International Journal of Hydrogen Energy* 46 (2021): 6225–6238, https://doi.org/10.1016/j.ijhydene.2020.11.150.

34. Z. Zhang, M. Ding, T. Cheng, et al., "Continuous Epitaxy of Single-Crystal Graphite Films by Isothermal Carbon Diffusion Through Nickel," *Nature Nanotechnology* 17 (2022): 1258–1264, https://doi.org/10.1038/s41565-022-01230-0.

35. A. Akbari, B. V. Cunning, S. R. Joshi, et al., "Highly Ordered and Dense Thermally Conductive Graphitic Films from a Graphene Oxide/Reduced Graphene Oxide Mixture," *Matter* 2 (2020): 1198–1206.

15214095, 0, Downloaded from https://advanced.onlinelibrary.wiley.com/doi/10.1002/adma.202518450 by Peking University Health, Wiley Online Library on [12/02/2026]. See the Terms and Conditions (https://onlinelibrary.wiley.com/terms-and-conditions) on Wiley Online Library for rules of use; OA articles are governed by the applicable Creative Commons License

36. X. D. Zhang, Y. Guo, Y. J. Liu, et al., "Ultrathick and Highly Thermally Conductive Graphene Films by Self-Fusion," *Carbon* 167 (2020): 249–255.

37. D. D. L. Chung, "Review Graphite," *Journal of Materials Science* 37 (2002): 1475–1489, https://doi.org/10.1023/A:1014915307738.

38. D. Pakhare and J. Spivey, "A Review of Dry (CO_2) Reforming of Methane Over Noble Metal Catalysts," *Chemical Society Reviews* 43 (2014): 7813–7837, https://doi.org/10.1039/C3CS60395D.

39. P. Boldrin and N. P. Brandon, "Progress and Outlook for Solid Oxide Fuel Cells for Transportation Applications," *Nature Catalysis* 2 (2019): 571–577, https://doi.org/10.1038/s41929-019-0310-y.

40. Q. Xu, Z. Guo, L. Xia, et al., "A Comprehensive Review of Solid Oxide Fuel Cells Operating on Various Promising Alternative Fuels," *Energy Conversion and Management* 253 (2022): 115175, https://doi.org/10.1016/j.enconman.2021.115175.

41. M. Singh, D. Zappa, and E. Comini, "Solid Oxide Fuel Cell: Decade of Progress, Future Perspectives and Challenges," *International Journal of Hydrogen Energy* 46 (2021): 27643–27674, https://doi.org/10.1016/j.ijhydene.2021.06.020.

42. K. Hong, M. Choi, Y. Bae, et al., "Direct Methane Protonic Ceramic Fuel Cells With Self-Assembled Ni-Rh Bimetallic Catalyst," *Nature Communications* 14 (2023): 7485, https://doi.org/10.1038/s41467-023-43388-8.

43. P. Fan, X. Zhang, D. Hua, and G. Li, "Experimental Study of the Carbon Deposition From CH_4 Onto the Ni/YSZ Anode of SOFCs," *Fuel Cells* 16 (2016): 235–243, https://doi.org/10.1002/fuce.201500038.

44. T. P. Wang, N. Sun, R. Z. Wang, et al., "One-Step Preparation of Large-Size 1.5-μm-Thick Robust YSZ Electrolyte for High CH_4 Conversion SOFCs at 600°C," *Separation and Purification Technology* 349 (2024): 127825, https://doi.org/10.1016/j.seppur.2024.127825.

45. S. T. Wismann, J. S. Engbæk, S. B. Vendelbo, et al., "Electrified Methane Reforming: A Compact Approach to Greener Industrial Hydrogen Production," *Science* 364 (2019): 756–759, https://doi.org/10.1126/science.aaw8775.

46. Z. Wu, P. Zhu, J. Yao, et al., "Combined Biomass Gasification, SOFC, IC Engine, and Waste Heat Recovery System for Power and Heat Generation: Energy, Exergy, Exergoeconomic, Environmental (4E) Evaluations," *Applied Energy* 279 (2020): 115794.

47. J. H. Myung, H. J. Ko, J. J. Lee, J. H. Lee, and S. H. Hyun, "Synthesis and Characterization of NiO/GDC–GDC Dual Nano-Composite Powders for High-Performance Methane Fueled Solid Oxide Fuel Cells," *International Journal of Hydrogen Energy* 37 (2012): 11351–11359, https://doi.org/10.1016/j.ijhydene.2012.04.140.

48. T. Razpotnik and J. Macek, "Synthesis of Nickel Oxide/Zirconia Powders via a Modified Pechini Method," *Journal of the European Ceramic Society* 27 (2007): 1405–1410, https://doi.org/10.1016/j.jeurceramsoc.2006.05.059.

49. F. Zhou, Y. H. Liu, X. F. Zhao, et al., "Effects of Cerium Doping on the Performance of LSCF Cathodes for Intermediate Temperature Solid Oxide Fuel Cells," *International Journal of Hydrogen Energy* 43 (2018): 18946—18954, https://doi.org/10.1016/j.ijhydene.2018.08.041.

Supporting Information

Additional supporting information can be found online in the Supporting Information section.

Supporting File: adma72482-sup-0001-SuppMat.docx.

15214095, 0, Downloaded from https://advanced.onlinelibrary.wiley.com/doi/10.1002/adma.202518450 by Peking University Health, Wiley Online Library on [12/02/2026]. See the Terms and Conditions (https://onlinelibrary.wiley.com/terms-and-conditions) on Wiley Online Library for rules of use; OA articles are governed by the applicable Creative Commons License